International Journal of Heat and Mass Transfer 70 (2014) 745–757

Contents lists available at ScienceDirect

International Journal of Heat and Mass Transfer

journal homepage: www.elsevier.com/locate/ijhmt

Phase change calculations for film boiling flows

Yeng-Yung Tsui *, Shi-Wen Lin, Yin-Nan Lai, Feng-Chi Wu

Department of Mechanical Engineering, National Chiao Tung University, Hsinchu 300, Taiwan, ROC

ARTICLE INFO

Article history:
Received 24 May 2013
Received in revised form 19 November 2013
Accepted 19 November 2013
Available online 14 December 2013

Keywords:
Film boiling
Two-phase flow
Phase change
VOF method
Numerical simulation

ABSTRACT

A new VOF based interface tracking method, termed CISIT, developed by the present authors recently is extended to include heat and mass transfer due to phase change. In this method, the interface is represented by the contour surface of VOF value 0.5. The interface is advanced in a conservative prediction-correction manner to ensure that the distribution of the VOF is a good approximation to the Heaviside function. An important issue related to the mass transfer across the interface is the treatment of the jump condition for the energy equation. The interface is tackled as an internal boundary for temperature field. The heat flux at the boundary is calculated separately in individual phase. However, unlike other studies, the energy equation for the two phases is solved simultaneously in an implicit way. This method is validated through tests on model problems for which theoretical solutions are available. Calculations are then performed to simulate boiling bubble flows emerging from a planar film and a circular film. The latter case also serves to demonstrate that the present methodology is applicable to phase change flows with irregular geometry. Different boiling modes are identified according to the superheated temperatures.

1. Introduction

The liquid–vapor flow can be found in many industrial and natural processes. A distinct character of this two-phase flow is the existence of an interface between different phases across which the forces acting on the fluids are in equilibrium. A certain amount of fluid is transferred from one phase to another when the temperature field is non-uniform and the fluids are saturated at the interface. Together with the mass transfer, large amounts of energy in the form of latent heat are released in the phase change.

Direct numerical simulation of the two-phase flow is not straightforward as the single phase flow. The following issues relating to the interface boundary separating the two phases require special attention: accurate representation of the interface, evolution of this boundary with time, unequal material properties between the different phases, and jump condition across the boundary. Treatments of these issues affect not only accuracy but also stability of the numerical calculation. A variety of methods had emerged to deal with interfacial flows in the past decades, some of which were extended to include heat and mass transfer processes for phase change. To simulate growth of vapor bubble, Welch [1,2] adopted moving and triangular meshes so that the interface can coincide with grid lines. Son and Dhir [3] made a coordinate transformation such that the interface is represented by a curvilinear coordinate line. These methods maintain the sharp feature of the interface. However, they are able to follow the bubble only for a short time before the bubble becomes greatly distorted or changes its topology such as breakoff.

The limitation to modest deformation of the interface can be released by using Eulerian grids, i.e., fixed grids. Juric and Tryggvason [4] and Esmaeeli and Tryggvason [5] investigate film boiling flows using the front tracking technique [6]. The fluid velocity field is calculated on a fixed grid while the phase boundary, represented by a surface grid, is moved in a Lagrangian manner. The surface grid needs to be re-meshing to maintain proper configuration during its advection. In general, the interaction between the two grid systems makes it difficult to implement, especially in three-dimensional problems.

An effective approach using fully fixed grids is to mark different phases by an indicator function. Two such indicators widely adopted are the VOF function and the level set function. Welch and Wilson [7] used a VOF based algorithm in connection with a mass transfer model to simulate the film boiling flow on a horizontal surface. Welch and Rachidi [8] extended this method to consider a conjugate problem between a solid wall and the boiling flow. The study of Agarwal et al. [9] provided more detailed insights into the film boiling process.

Son and Dhir [10] applied the level set method to examine the effects of wall superheat on the bubble release during film boiling near critical conditions. In another study by Son et al. [11], the growing and departure of a bubble from a horizontal surface in the nucleate boiling regime was under consideration. Later, the formulations of the method for phase change were modified by Son [12]. Numerical instability is quite likely encountered at the phase boundary owing to the discontinuity of material properties. A practice often employed to overcome this problem is to diffuse this boundary artifi-

* Corresponding author. Tel.: +886 3 5131556; fax: +886 3 5720634.
E-mail address: yytsui@mail.nctu.edu.tw (Y.-Y. Tsui).

0017-9310/$ - see front matter © 2013 Elsevier Ltd. All rights reserved.
http://dx.doi.org/10.1016/j.ijheatmasstransfer.2013.11.061

Nomenclature

C	specific heat
e	specific energy
$\vec{g}, g$	gravitational acceleration
Gr	Grashof number ($=\rho_v(\rho_l-\rho_v)g\lambda^3/\mu_v^2$)
h_{lv}	latent heat of evaporation
Ja	Jacob number ($=C_v(T_w-T_{sat})/h_{lv}$)
Ja^*	modified Jacob number
k	thermal conductivity
$\dot{m}$	mass flux
$\vec{n}$	unit normal vector
Δn	normal distance away from the interface
Nu	Nusselt number
$\overline{Nu}$	space and time averaged Nusselt number
P	pressure
Pr	Prandtl number ($=C_v\mu_v/k_v$)
$\dot{q}$	heat release rate
$\vec{S}_f^w$	surface vector of wetted area on cell face
$\vec{S}_m, S_M$	source terms in momentum and mass equations
T	temperature
t	time
Δt	time step size
$\vec{V}$	velocity vector
Δv	cell volume
x, y	Cartesian coordinates

Greek symbols

α	VOF function
δ	interface location in 1-D model problems
κ	mean curvature
λ	characteristic length for film boiling
λ_o	most dangerous Taylor wave length
μ	viscosity
ρ	density
σ	surface tension coefficient
$\bar{\bar{\tau}}$	viscous stresses

Subscripts

f	cell face
fj	jth cell face
int	interface
l	liquid phase
P	primary cell
sat	saturation state
v	vapor phase
w	wall value

Superscripts

n	new time step
o	old time step

cially by introducing smoothed delta functions [4,13]. With this procedure, however, there are some difficulties in imposing jump conditions for energy accurately in the diffused region. A recent progress in the level set method is to incorporate the ghost fluid method [14,15] in dealing with jump conditions to preserve the sharp contact discontinuity. The method introduces ghost nodes on the two sides of the interface and information pertaining to one phase is extrapolated to the ghost points on the other side of the discontinuity. This approach was adopted by Tanguy et al. [16], Gibou et al. [17], Son and Dhir [18], and Maurya et al. [19] to solve the energy equation in phase change flows.

It is recognized that the fluid mass is not conserved by the level set methods while the accuracy of VOF methods is highly dependent upon the calculation of interface normal and curvature from volume fractions. Advanced methods appear by combining the two techniques to compensate each other. The use of such an approach in the study of film boiling flow was given by Guo et al. [20].

Comparing with the level set methods, the VOF methods are more difficult to implement due to the difficulties to reconstruct the interface from the VOF function and to advect this interface surface, which is especially serious in three-dimensional problems. In a recent study of present authors [21], a simple and robust VOF based method, termed conservative interpolation scheme for interface tracking (CISIT), was developed to address the above problems. In the present work, this method is extended to consider heat and mass transfer in phase change flows. Different from the ghost fluid methods, the energy jump condition is tackled by an interpolation procedure in the interface cells to preserve the sharp gradient feature.

2. Mathematical formulation

2.1. Governing equations

It is assumed that the flows in both phases are incompressible and in the laminar regime with constant thermodynamic properties. The governing equations are given in the following conservation form.

$$\nabla\cdot\vec{V}=S_M \tag{1}$$

$$\frac{\partial\rho\vec{V}}{\partial t}+\nabla\cdot(\rho\vec{V}\otimes\vec{V})=-\nabla P+\nabla\cdot\bar{\bar{\tau}}+\rho\vec{g}+\vec{S}_m \tag{2}$$

$$\frac{\partial\rho e}{\partial t}+\nabla\cdot(\rho\vec{V}e)=\nabla\cdot\left(\frac{k}{C}\nabla e\right) \tag{3}$$

where $\vec{V}$ is the velocity, ρ the density, e the specific energy, P the pressure, k the thermal conductivity, C the specific heat, and $\bar{\bar{\tau}}$ the viscous stress. The sources S_M and $\vec{S}_m$ in the mass and momentum equations are generally zero except in the cells containing the interface where jump conditions must be taken into account.

2.2. Jump conditions at interface

Consider a conserved property ϕ governed by the hyperbolic conservation law.

$$\frac{\partial\phi}{\partial t}+\frac{\partial f}{\partial x}=0 \tag{4}$$

where f is a flux function of ϕ. In the x–t plane, suppose there is a curve $x_s(t)$ across which ϕ is discontinuous, but ϕ is continuous on either side of the curve. Integration of this equation leads to the Rankine–Hugoniot conditions or the jump conditions.

$$[\phi]V_s=[f] \tag{5}$$

where $[\cdot]$ denotes the difference across the discontinuity and $V_s = dx_s/dt$ is the speed of the curve. In multi-dimensions, the corresponding jump conditions are

$$[\phi]\vec{V}_{\text{int}}\cdot\vec{n}=[\vec{f}]\cdot\vec{n} \tag{6}$$

where $\vec{V}_{\text{int}}$ is the interface velocity and $\vec{n}$ the unit vector normal to the interface. After application to the continuity, momentum and

energy equations, and some manipulations, the following results are yielded.

$$\dot{m}_{\text{int}} = \rho_v(\vec{V}_v - \vec{V}_{\text{int}}) \cdot \vec{n} = \rho_l(\vec{V}_l - \vec{V}_{\text{int}}) \cdot \vec{n} \tag{7}$$

$$(P_v - P_l)\tilde{\tilde{I}} \cdot \vec{n} - (\tilde{\tilde{\tau}}_v - \tilde{\tilde{\tau}}_l) \cdot \vec{n} + \dot{m}_{\text{int}}(\vec{V}_v - \vec{V}_l) = \sigma\kappa\vec{n} \tag{8}$$

$$\dot{q}_{\text{int}} = \dot{m}_{\text{int}}(C_v T_v - C_l T_l) = \left[-(k\nabla T)_v + (k\nabla T)_l\right] \cdot \vec{n} \tag{9}$$

where $\dot{m}_{\text{int}}$ is the mass flux across the interface due to phase change, $\dot{q}_{\text{int}}$ the heat release rate, σ the surface tension coefficient, and κ the mean curvature. The subscripts l and v denote the liquid and vapor phases.

In the momentum jump condition shown in Eq. (8), the term on the right-hand side is added to account for the surface tension effect. It can be seen that the normal projection of the equation is reduced to the Young–Laplace equation by ignoring the viscous stress and the momentum terms. The surface tension can be regarded as a surface pressure $P_s(=P_v - P_l)$. According to Brackbill et al. [22], this surface force can be converted into the form of body force. As a result, the source term in Eq. (2) is given by

$$\vec{S}_m = \sigma\kappa\nabla\alpha \tag{10}$$

where α is the VOF function. The curvature of the interface can be expressed in terms of the divergence of the unit normal vector to the interface.

$$\kappa = -\nabla \cdot \left(\frac{\nabla\alpha}{|\nabla\alpha|}\right) \tag{11}$$

which can be rearranged into the following form.

$$\kappa = \frac{1}{|\nabla\alpha|}\left[\left(\frac{\nabla\alpha}{|\nabla\alpha|} \cdot \nabla\right)|\nabla\alpha| - \nabla \cdot \nabla\alpha\right] \tag{12}$$

It is assumed that both the temperatures of the liquid and vapor at the interface are of the same and equal to the equilibrium saturation temperature corresponding to the system pressure ($T_{int} = T_{sat}(P_0)$). Thus, Eq. (9) can be rewritten as

$$\dot{q}_{\text{int}} = \dot{m}_{\text{int}} h_{lv} = -\left(k\frac{\partial T}{\partial n}\right)_v + \left(k\frac{\partial T}{\partial n}\right)_l \tag{13}$$

where h_{lv} is the latent heat of evaporation.

It is more convenient and clearer to consider the integral form of the continuity equation for a computational cell containing the interface.

$$\int_{Sc} \vec{V} \cdot \vec{n} ds = \int_{Si} (\vec{V}_v - \vec{V}_l) \cdot \vec{n} ds \tag{14}$$

where *Sc* is the surface of the considered cell and *Si* the phase interface within the cell. The difference between the velocities of the two phases can be obtained from substitution of Eq. (13) into Eq. (7).

$$(\vec{V}_v - \vec{V}_l) \cdot \vec{n} = \left(\frac{1}{\rho_v} - \frac{1}{\rho_l}\right)\frac{\dot{q}_{\text{int}}}{h_{lv}} \tag{15}$$

Therefore, the source term of the continuity equation (1) is given by

$$S_M = \frac{1}{\Delta v}\left(\frac{1}{\rho_v} - \frac{1}{\rho_l}\right)\int_{Si} \frac{\dot{q}_{\text{int}}}{h_{lv}} ds \tag{16}$$

where Δv denotes the volume of the cell.

2.3. VOF equation and smoothing of properties

In the VOF method, the location of the phase boundary is determined by tracking the volume fraction α in the flow field. This indicator function is either unity or zero in the cells containing a single phase and becomes a value between one and zero in the interface cells. With the assumption of incompressible flow, the advection equation for the VOF function can be cast into the conservation form.

$$\frac{\partial\alpha}{\partial t} + \nabla \cdot (\vec{V}\alpha) = 0 \tag{17}$$

It is known that large gradients of density and viscosity in the interface region may cause numerical instability in the velocity field. To soothe this problem, artificial smoothing becomes necessary. These properties are calculated from a smoothed VOF function α^* as

$$\rho^* = \alpha^*\rho_v + (1 - \alpha^*)\rho_l \tag{18a}$$

$$\mu^* = \alpha^*\mu_v + (1 - \alpha^*)\mu_l \tag{18b}$$

Different from common approaches adopted by other studies using a variety of smoothing functions in the region around the interface, an averaging smoothing technique is employed to smear this function. First, the VOF values at grid nodes are estimated by interpolation from the cell centroids where they are stored. Then, a new α at each cell centroid is obtained by averaging over the values on its cell vertices. In this way, the interface region is expanded to the two adjacent cells on either side of the interface cell. Two such smoothing processes are generally taken in the calculation to enhance smearing effects.

In summary, the resulting forms of the mass balance and momentum equations are

$$\nabla \cdot \vec{V} = \frac{1}{\Delta v}\left(\frac{1}{\rho_v} - \frac{1}{\rho_l}\right)\int_{Si} \frac{\dot{q}_{\text{int}}}{h_{lv}} ds \tag{19}$$

$$\frac{\partial\rho^*\vec{V}}{\partial t} + \nabla \cdot (\rho^*\vec{V} \otimes \vec{V}) = -\nabla P + \nabla \cdot \tilde{\tilde{\tau}}^* + \rho^*\vec{g} + \sigma\kappa\nabla\alpha^* \tag{20}$$

In this formulation, the smoothed density and viscosity are used in the momentum calculation and in the estimation of surface tension. For temperature field the discontinuity in the properties are preserved for the purpose to predict the heat release rate $\dot{q}_{\text{int}}$ accurately.

3. Numerical methods

3.1. Interface tracking

The most popular method in the VOF category is the PLIC algorithm due to Youngs [23]. The interface is represented by piecewise linear curves which are discontinuous across computational cells. The reconstruction of the interface from the VOF is not straightforward by this algorithm. Besides, the procedure to advance the interface is complicated because it is needed to consider a large number of possibilities of interface configuration in approximating the flux across cell faces. These difficulties can be overcome by a newly developed algorithm called CISIT [21]. In this method, the interface is represented by the contour line (or contour surface in 3D) of VOF value 0.5, which can easily be constructed by interpolation practices. It is followed by a conservative prediction–correction procedure to advance the interface through the computational grid. A brief discussion is introduced in the following. More details are given in the referred article.

The values of the volume fraction are stored at the centroids of computational cells. An interpolation practice is carried out to find this function on the grid nodes. It is followed by examining the two end nodes of all the edges of each cell. The interface crosses the edge if the volume fraction of one of the nodes is less than 0.5

and the other greater than 0.5. A continuous piecewise linear interface is built after this process proceeds in all cells.

An interface cell is shown in Fig. 1. The surface wetted by a fluid is denoted by $\vec{s}_f^w$. The wetted surfaces form inlets and outlets to the cell for the fluid. The conservation of fluid mass for the cell leads to

$$\frac{\Delta v}{\Delta t}(\alpha_P^n - \alpha_P^o) + \sum_j \vec{V}_{fj} \cdot \vec{s}_{fj}^w = 0 \tag{21}$$

This calculation performs well when the interface remains in the cell during the time marching. However, problems arise when the interface moves across the cell boundaries. Four situations need to be considered.

(a) Over filling ($\alpha_P > 1$)
Suppose a uniform velocity field prevails in a cell shown in Fig. 2(a), when the interface is going to advance into the neighboring cell. The new time value of α_p predicted by Eq. (21) becomes greater than 1 since the sum of the inlet wetted areas on the west and south sides ($\vec{S}_W^w$ and $\vec{S}_S^w$) is greater than the outlet wetted area on the east side ($\vec{S}_E^w$). To force the interface to move across the cell boundary, the excessive fluid $\alpha_P - 1$ must be reallocated to the downstream cells N_E and N_N. The portioning of the mass is based on the ratio of the efflux through the corresponding face to the total efflux.

(b) Under filling ($\alpha_P < 1$)
There is a possibility in shear flows that the new value of α_p remains less than 1 as the interface advances to leave the cell. Since the interface is not existent in the cell any more, the VOF value remains unchanged in later time. Therefore, when the VOF values on the all the vertices of the cell are greater than 0.5 (i.e., the interface is not located in the cell) and α_P becomes less than 1, fluid is retrieved from the downstream cells to fill this cell such that α_P is equal to 1.

(c) Over depleting ($\alpha_P < 0$)
In contrast to the over filling, retreat of the interface from the cell leads to $\alpha_P < 0$ (see Fig. 2(b)). The over depleted fluid must be retrieved from the downstream cells. The portioning of the mass is similar to that for the over filling.

(d) Under depleting ($\alpha_P > 0$)
In strong shear flows, it is possible for α_P to remain greater than 0 as the interface retreat from the cell. Similar to the under filling, the mass will remain in this cell. Hence, whenever it is found that the VOF values for all the vertices of the cell are less than 0.5 (i.e., no interface in the cell) and $\alpha_P > 0$, fluid in this cell must be allocated to the downstream cells so that α_P becomes zero.

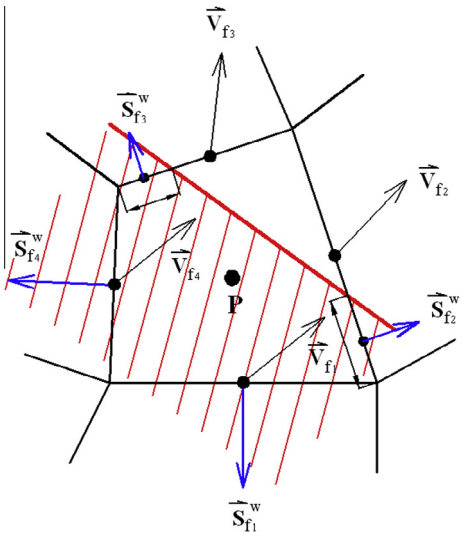

Fig. 1. A control volume partially filled with fluid.

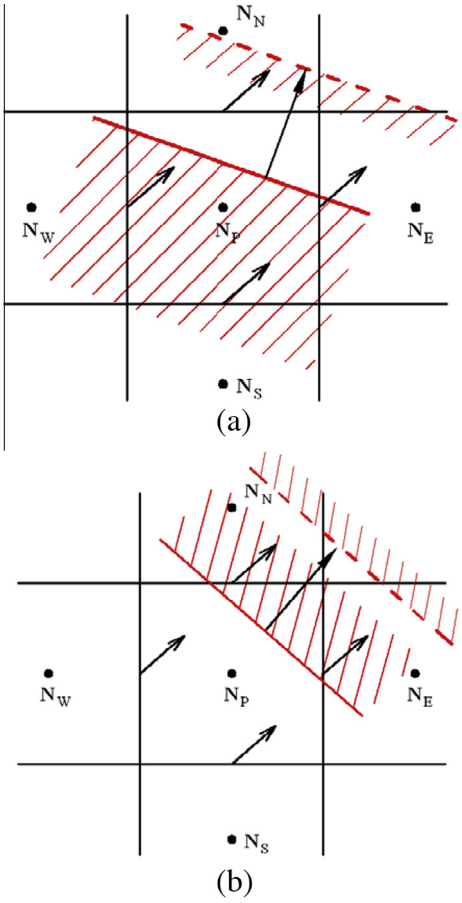

Fig. 2. Moving of the interface across a control volume: (a) advancing; (b) retreating.

After one sweep of such corrections, some neighboring cells may be over filled or over depleted. Hence, two correction steps are undertaken to ensure no overshoots and undershoots in the VOF field.

3.2. Numerical methods for velocity and temperature fields

The transport equations are discretized using a finite volume method suitable for unstructured meshes [24]. The convection term is approximated using the Van Leer scheme arranged in the flux limiter form [25,26]. The coupling between momentum and continuity equations is treated in a non-iterative, predictor–corrector algorithm [27].

An important issue related to the mass transfer across the interface is to treat the jump condition for energy. As seen from Eq. (13), the estimate of the normal gradients for temperature on both sides of the interface is required. The temperature gradients are generally discontinuous. Any attempt to smooth this discontinuity will distort the mass transfer rate. Therefore, these gradients must be discretized by one-sided difference. As indicated previously, the interface temperature is assumed to be saturated at the system pressure. The heat release rate can be approximated by

$$\dot{q}_{\text{int}} = -k_v \frac{T_v - T_{\text{int}}}{\Delta n} + k_l \frac{T_{\text{int}} - T_l}{\Delta n} \tag{22}$$

where T_v and T_l are the temperatures of the two phases at a normal distance Δn away from the interface, which are obtained by linear

interpolation from the surrounding nodal temperatures. The interface is regarded as an internal boundary for the temperature field. For the cells next to the interface cell to see proper temperature gradients an interpolation practice is conducted to find the temperature at the nearby points using the gradients. As shown in Fig. 3, two situations need to be considered. The cell centroid is located in the considered phase (vapor phase in Fig. 3(a)) in the first and located in the other phase in the second (Fig. 3(b)). It is the temperature T_P at the cell centroid and the temperature T_f at the cell face needed to be calculated. They are estimated using T_{int} and the temperature gradient at the interface $(\partial T/\partial n)_v$. These temperatures form Dirichilet boundary conditions for the considered phase. Similar treatments can be conducted for the other phase. Unlike other studies, in which the energy equation is solved using the explicit scheme, the fully implicit scheme is adopted in our calculations, which can be expressed as

$$A_P T_P = \sum A_C T_C + S \tag{23}$$

where the subscript c denotes the surrounding cell values. In order to fix the temperature T_P at the interface cell, the following settings are specified.

$$A_P = C, \quad A_C = 0, \quad S = CT_P \tag{24}$$

where C is a great number.

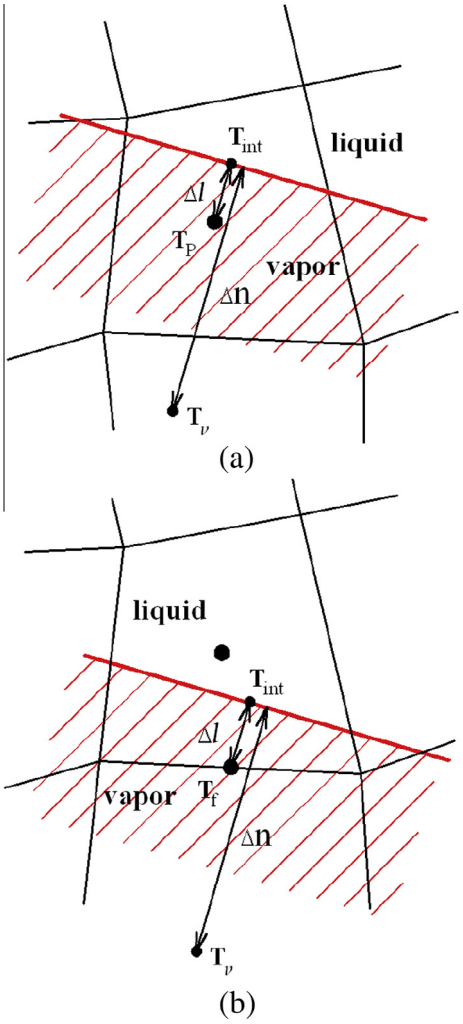

Fig. 3. Illustration for calculation of temperatures at (a) cell centroid and (b) cell face.

The overall solution procedure is summarized as follows.

1. With the prevailing temperature, the temperature gradients on the two sides of the interface are calculated and, then, the temperatures on the interface cell are obtained.
2. The energy equation is solved to yield new temperature field.
3. The temperature gradients at the interface are recalculated. It gives the mass transfer rate.
4. The momentum equation is solved, followed by adjustment of the velocity and pressure via enforcement of mass continuity.
5. New VOF values are sought by the CISIT method. The interface is then reconstructed.

This completes calculations in one time step. The same procedure is repeated in the following time steps.

4. Results and discussion

The method described above is first validated through tests on two model problems for which theoretical solutions are available. One is a melting problem and the other a solidification problem. They can be considered as evaporation of saturated liquid and superheated liquid problems. It is followed by simulating realistic flows including film boiling on a horizontal surface and on a circular cylinder.

4.1. 1-D evaporation of saturated liquid

Consider a liquid, initially at its saturated temperature T_{sat}, exposed to a heated wall at temperature T_w located at $x = 0$, as shown in Fig. 4(a). Evaporation of the liquid into vapor causes the phase boundary to move in the x-direction. It is assumed that the vapor speed is zero. The temperature in the vapor region is governed by Fourier's equation with the following boundary and jump conditions.

$$T(x = 0) = T_w, \quad T(x = \delta(t)) = T_{sat} \tag{25a}$$

$$\rho V_{int} h_{lv} = -k_v \left.\frac{\partial T}{\partial x}\right|_{x=\delta(t)} \tag{25b}$$

This is equivalent to the melting problem for a saturated solid in [28], for which similarity solution can be found.

In simulations, the thermodynamic properties are: $C = 0.2$ kJ/(kg-K), $h_{lv} = 10$ kJ/kg, and two different thermal diffusivities $\alpha_v = 2.5 \times 10^{-3}$ and 2.5×10^{-2} m^2/s corresponding to density ratios 100 and 1000. The temperature difference between T_w and T_{sat} is 10 °C. The grid size is 0.2 mm and the initial phase boundary is located at 0.3 mm. The initial temperature profile in the vapor region is assumed to be linear. In this one-dimensional problem, the centroid of the cell occupied by the phase interface is located in the liquid phase side as the VOF is greater than 0.5 and located in the vapor phase side for VOF less than 0.5. Thus, it is the temperature at the centroid for the former and the temperature at the cell face for the latter needed to be estimated using the interpolation procedure described above. Fig. 5 shows the interface position as well as the interface speed. The agreement with the theoretical solution is excellent.

4.2. 1-D evaporation of superheated liquid

It is seen that accurate results are obtained in the above simulation despite very few cells used to describe the temperature profile in early stage. This is due to the nearly linear variation of the exact solution because the Jacob number $Ja(=C_v(T_w - T_{sat})/h_{lv})$ is small. In the second case, a liquid, initially at superheated temper-

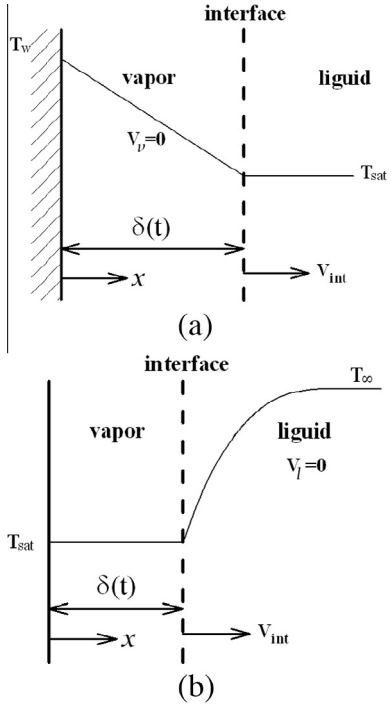

Fig. 4. Illustration for the problem: (a) evaporation of saturated liquid; (b) evaporation of superheated liquid.

ature T_∞, is in contact with a vapor at saturated temperature T_{sat}. Vaporization at the phase boundary causes its retreat in the x-direction, as seen in Fig. 4(b). A thermal boundary layer is formed in the liquid phase near the interface, resulting in a steep temperature gradient and rendering this problem more difficult to predict accurately. The case considered here is different from the one used by Welch and Wilson [7], in which zero vapor velocity was assumed and, thus, the liquid velocity is set by the evaporation rate. This leads to a convection–diffusion equation for which no closed-form solution is available. In his study, the velocity of the liquid is assumed to be zero. In this way, the transport of temperature in the liquid is governed by diffusion only, subject to the following conditions.

$$T(x=0)=T_{sat}, \quad T(x=\infty)=T_\infty \tag{26a}$$

$$T(t=0)=T_\infty, \quad \delta(t=0)=0 \tag{26b}$$

$$\rho V_{\text{int}} h_{lv} = -k_v \left.\frac{\partial T}{\partial x}\right|_{x=\delta(t)} \tag{26c}$$

It is equivalent to the solidification problem for a supercooled liquid in [28] and theoretical solution is available.

Thermodynamic properties for the liquid are assumed to be: C = 200 kJ/(kg-K), h_{lv} = 165 kJ/kg, and α_l = 0.25 m^2/s. The temperature of the liquid is 0.5 °C higher than the saturated temperature initially. The initial location of the phase boundary is set at 0.1 m. Theoretical temperature profile at t = 0.1 s is used as initial condition for numerical calculations. Comparison of interface location, interface velocity and temperature at t = 10 s with exact solution is made in Fig. 6. It is obvious that the agreement with theoretical results is improved as the grid size is reduced from 0.1 to 0.025 m. Oscillations in the interface velocity are visible, which occurs whenever the interface moves from one cell to another cell. It can also be seen that the oscillation amplitude dwindles with the mesh size.

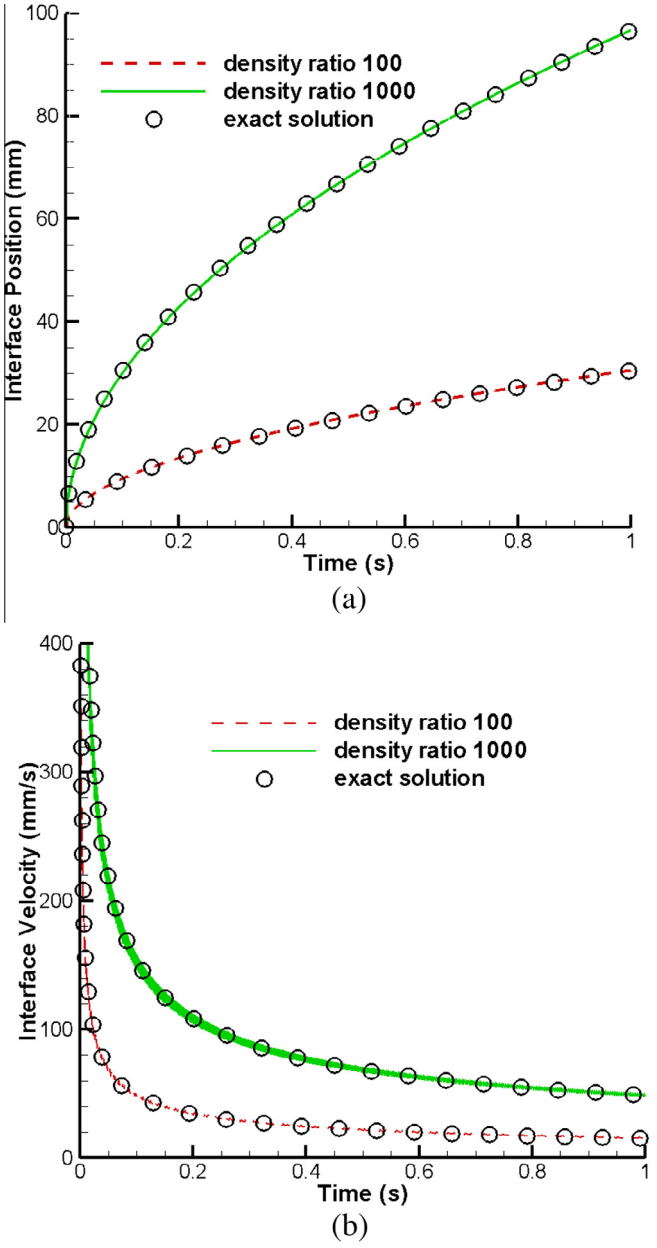

Fig. 5. (a) Interface position and (b) interface velocity for the evaporation of saturated liquid problem.

4.3. Film boiling on a horizontal surface

The first two-dimensional simulation of phase change is carried out by considering the boiling of water on a horizontal surface. The water is in a state (P = 21.799 MPa and T = 373 °C) near the critical point. The properties of the liquid water are given by ρ_l = 402.4 kg/m^3, k_l = 0.5454 W/(m-K), $\mu_l = 4.67\times10^{-5}$ Pa-s, $C_l = 2.18\times10^2$ kJ/kg-K and those for the water vapor are ρ_v = 242.7 kg/m^3, k_v = 0.5383 W/(m-K), $\mu_v = 3.24\times10^{-5}$ Pa-s, $C_v = 3.52\times10^2$ kJ/kg-K. The latent heat is h_{lv} = 276.4 kJ/kg and the surface tension $\sigma = 7\times10^{-5}$ N/m. Taking advantage of the flow symmetry, the width of the computational domain is chosen to be $\lambda_o/2 (\lambda_o = 2.3$ mm), where $\lambda_o = 2\pi\sqrt{3\sigma/(\rho_l-\rho_v)g}$ is the most dangerous Taylor wave length [29]. The height of the domain is λ_o. The flow field is made up of a superheated vapor film underneath a bulk of saturated water. The initial interface is perturbed and placed at $y = \lambda_o[2+\cos(2\pi x/\lambda_o)]/128$. The top boundary is

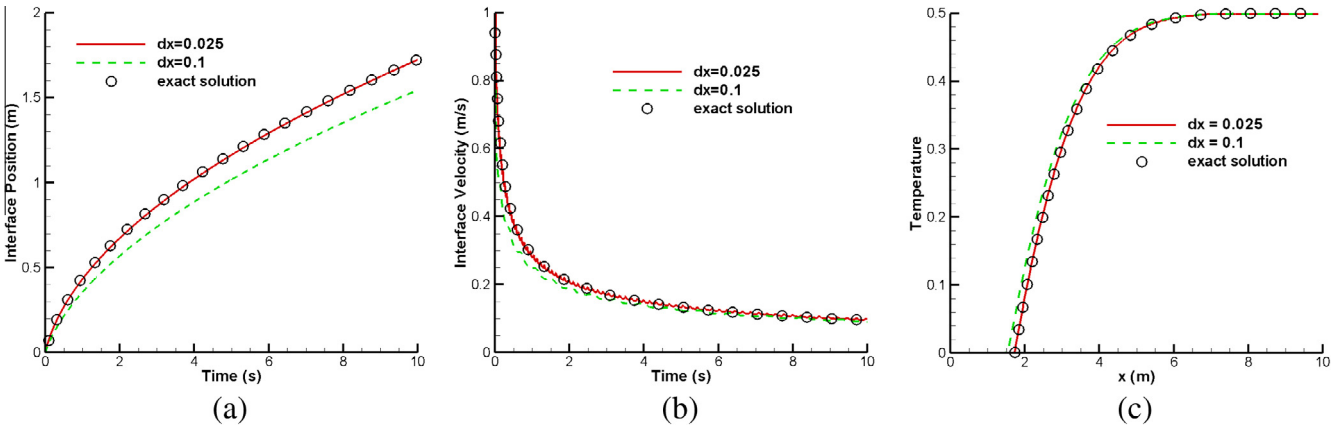

Fig. 6. (a) Interface position, (b) interface velocity and (c) temperature distribution at $t = 10$ s for the evaporation of superheated liquid problem.

open to allow fluid to enter or leave. Symmetrical conditions are imposed at the two side boundaries. The bottom wall is kept at certain temperatures above the saturated temperature. The initial temperature in the vapor film varies linearly from the wall to the phase interface.

In the convergence test, four different grids are used, viz., 90×180, 120×240, 180×360 and 240×480. It is shown below that for the case with superheated wall temperature of 10 °C, the flow will develop into a periodic state. The time periods of the cyclic pattern corresponding to the four different grids are 0.184, 0.185, 0.188, and 0.189. The overall average Nusselt numbers at the heated wall are 5.17, 5.34, 5.43, and 5.5. Apparently, the results for the second finest mesh are very close to those for the finest mesh. It is this grid used in the following simulations.

Fig. 7 shows time variation of the Nusselt number averaged over the heated wall, being defined by

$$Nu = \frac{1}{L}\int_0^L \frac{\lambda}{(T_w - T_{sat})}\frac{\partial T}{\partial n}\bigg|_w dx \tag{27}$$

where L is the length of the heated wall $(\lambda_o/2)$, $\lambda = \sqrt{\sigma/(\rho_l - \rho_v)g}$ is a characteristic length and the subscript w denotes the wall value. Six different superheated wall temperatures are under consideration. At the lowest superheat ($\Delta T = 10$ °C), the temporal variation of Nu is nearly periodic after the effect of initial condition dimin-

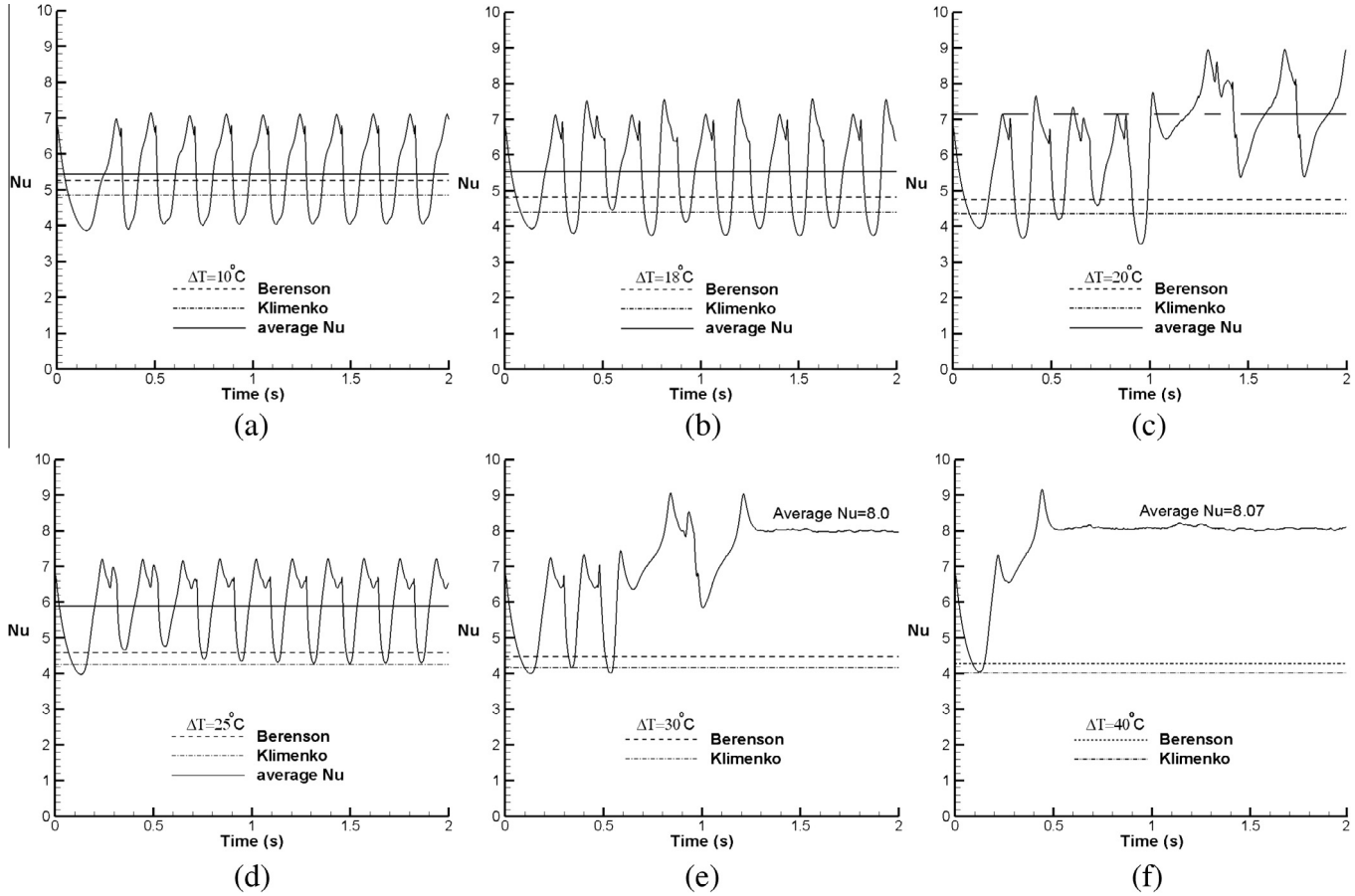

Fig. 7. Variation of Nusselt number for planar film boiling: (a) $\Delta T = 10$ °C; (b) $\Delta T = 18$ °C; (c) $\Delta T = 20$ °C; (d) $\Delta T = 25$ °C; (e) $\Delta T = 30$ °C; (f) $\Delta T = 40$ °C.

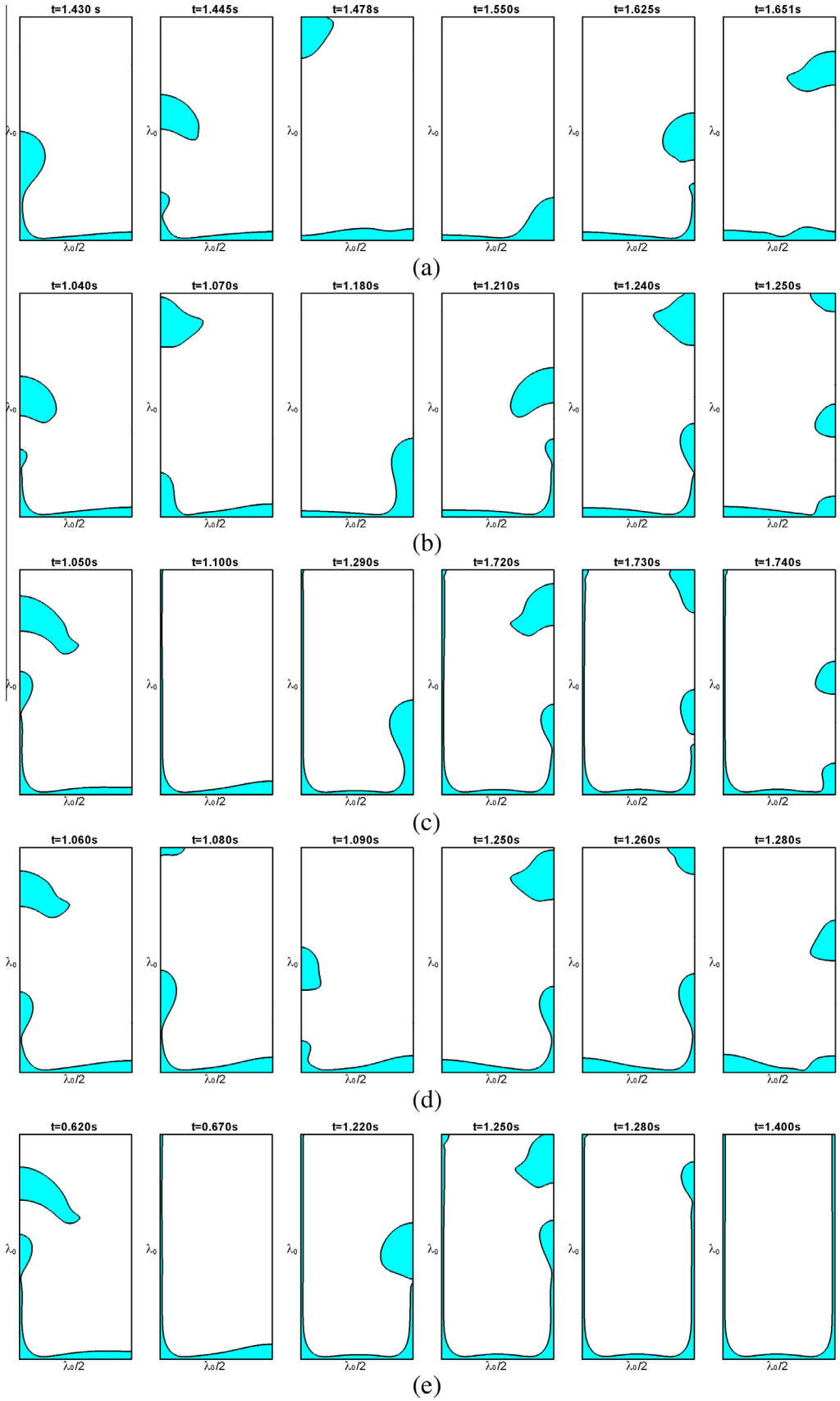

Fig. 8. Planar film boiling process: (a) ΔT = 10 °C; (b) ΔT = 18 °C; (c) ΔT = 20 °C; (d) ΔT = 25 °C; (e) ΔT = 30 °C.

ishes. It can be seen from Fig. 8(a) that a bubble is first formed at the left boundary. After the bubble is detached, the residual stem retreats due to the restoring force of surface tension. It can be identified from the plot at t = 1.478 s that a capillary wave propagates in

the transverse direction from the left side towards the right side. It is followed that another bubble release cycle proceeds on the right boundary. To illustrate the flow field, velocity vectors are plotted every several grid nodes in Fig. 9. The buoyancy brings about an upward flow in the rising bubble and induces a clockwise vortex at the gas/liquid interface. After the bubble pinches off, the vapor stem drops down. It can be seen that the downward flow in the stem head induces a counterclockwise vortex. As noticed before, a capillary wave is formed at $t = 1.478$ s, causing a strong transverse flow towards the right under the film. This, in turn, results in an elongated vortex above the film, rotating counterclockwise. A clockwise vortex is formed at the right corner. At a later time, a bubble is developed at the right boundary and the same process is repeated.

As the superheated temperature is increased to 18 °C (see Fig. 7(b)), the periodic variation of *Nu* is not so regular. The variation behavior is slightly different in each two consecutive cycles. The cause of this phenomenon can be seen from Fig. 8(b). Only one bubble is generated on the left side of boundary. As for the right side, after a bubble breaks off, a second bubble grows up until it is finally released.

For $\Delta T = 20$ °C discrete bubbles break off from the two side boundaries alternatively in a less regularly periodic manner in the early stage. It is seen from Fig. 7(c) that after $t = 1.1$ s, the Nusselt number is changed to a higher level and a different cyclic pattern appears with a larger cyclic period. Fig. 8(c) shows that a steady-state vapor jet is formed at the left boundary whereas bubble release pattern still prevails at the other side. Two discrete bubbles can be viewed on the right boundary.

It is rather surprised to find from Fig. 7(d) that the periodic variation of *Nu* return to a more regular form when ΔT is increased to 25 °C. This result is owing to the regular release of two bubbles each time on both side boundaries, as shown in Fig. 8(d).

Further increase of the superheated temperature to 30 °C gives Figs. 7(e) and 8(e). Alternative bubble release takes place first, followed by formation of a vapor jet at the left boundary. Then, the bubble flow on the right boundary is transformed into a jet as well when time is greater enough. Even greater superheat of $\Delta T = 40$ °C leads to a quicker formation of the steady-state, double-jet pattern, which can be identified in Fig. 7(f).

To illustrate heat transfer at the heated wall, the distribution of Nusselt number along the wall at various times is presented in Fig. 10. In a thin film, the temperature varies in approximately linear manner from the wall temperature to the saturated temperature. Thus, it is expected that heat transfer is higher at the location where the film is thinner and vice versa. For $\Delta T = 10$ °C the change of bubble release from the left boundary to the right boundary can be identified from the observation of the shift of curve peak from left to right. For $\Delta T = 30$ °C it can be seen that after the transient stage, the curve finally becomes nearly symmetrical to the centerline with a peak on each side. This double-peak form simply reflects the double-jet flow pattern.

Both Berenson [29] and Klimenko [30] developed semi-empirical models for film boiling on a horizontal surface. Berenson [29] assumed that the vapor bubbles are spaced regularly. The distance between the bubbles and their diameters are proportional to the critical wavelength of the Taylor instability, which gives the following correlation.

$$Nu = C[Gr \times Pr/Ja]^{1/4} \tag{28}$$

Here C is a constant value 0.425, and *Nu*, *Gr*, *Pr*, and *Ja* are the Nusselt number, Grashof number, Prandtl number, and Jacob number, respectively.

$$Gr = \frac{\rho_v(\rho_l - \rho_v)g\lambda^3}{\mu_v^2} \tag{29a}$$

$$Pr = \frac{C_v\mu_v}{k_v} \tag{29b}$$

$$Ja = \frac{C_v(T_w - T_{sat})}{h_{lv}} \tag{29c}$$

Based on similar assumptions, Klimenko [30] extended the analysis to turbulent regime by using the Reynolds analogy.

The space and time averaged Nusselt numbers $\overline{Nu}$ obtained from the current simulations and the correlations of Berenson and Klimenko are compared in Fig. 7 and Table 1. The computed mean Nusselt number for $\Delta T = 20$ °C is the value averaged over the single-jet pattern period and those for $\Delta T = 30$ and 40 °C are

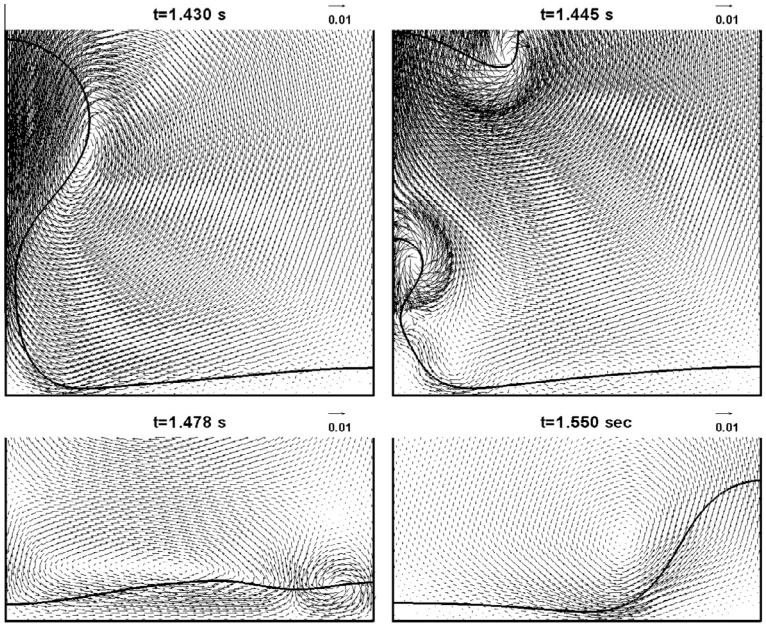

Fig. 9. Velocity vectors of the planar film boiling for $\Delta T = 10$ °C.

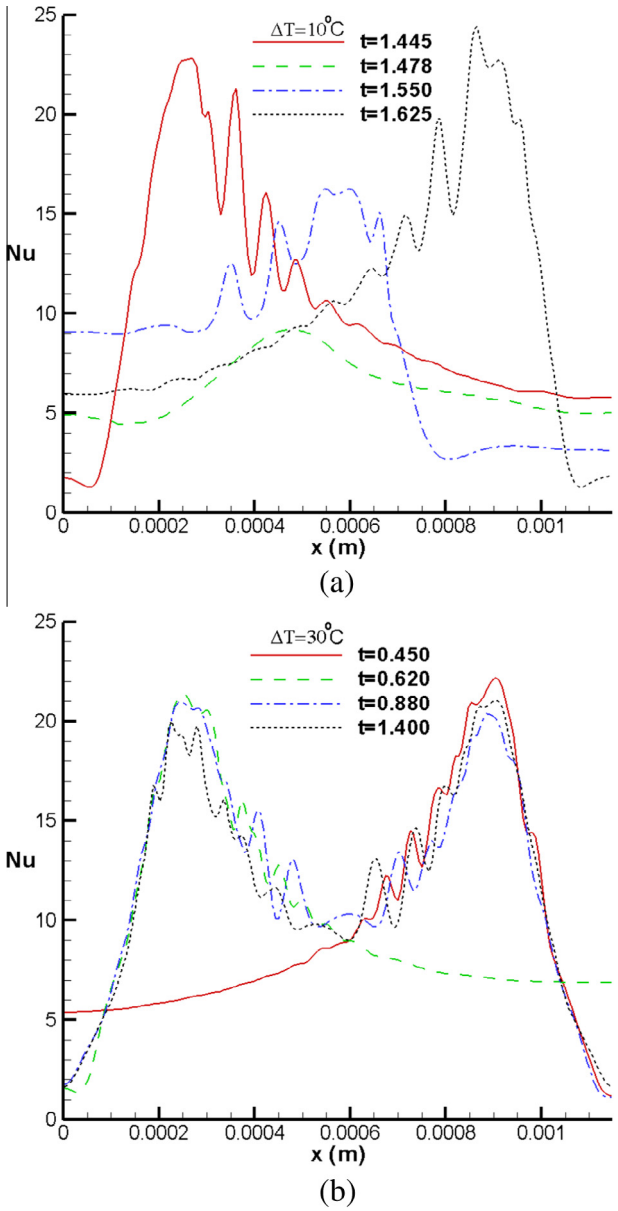

Fig. 10. Variation of heat flux along the heated wall: (a) $\Delta T = 10$ °C; (b) $\Delta T = 30$ °C.

the mean values in the double-jet pattern period. The thermodynamic properties for calculating the correlations are taken at the mean film temperature $((T_w + T_{sat})/2)$. It is noted that instead of Ja, a modified Jacob number $Ja^* = Ja/(1 + 0.34Ja)$ is used in the correlations of Berenson and Klimenko to account for sensible heat transfer. The use of original Ja will leads to smaller Nu, being especially serious for the Berenson's model at large superheats. The agreement of the calculation with Berenson's model is excellent for $\Delta T = 10$ °C. The deviation from Klimenko's correlation is within 12%. However, the difference increases with the superheat, which is especially serious in the jet modes.

Further comparison is given in Fig. 11. The temperature intervals for the five boiling patterns identified in Fig. 8 are specified. At the low temperatures less than 15 °C, single-bubble mode prevails, for which a single bubble is formed on either side of the boundary. For ΔT between 15 °C and 19 °C, it changes to the singe/multiple-bubble mode. In this mode, a single bubble is seen on one side and multiple bubbles are found on the other side. It is noted that two bubbles are detected for $\Delta T = 18$ °C in Fig. 8(b). However, three bubbles had been seen in the case with $\Delta T = 17$ °C. The single-jet mode falls in the range from 19 °C to 22 °C where a single jet is formed on one side, with discrete bubble released on the other side. The double-bubble mode is in the interval 22–27 °C, with two consecutive bubbles generated on either side. Steady state is reached and the double jet-mode is obtained when ΔT becomes higher than 27 °C. Compared with the correlations, the agreement is favorably reasonable in the first two modes, especially for the single-bubble mode. The deviation between simulations and theories becomes significant when vapor jet pattern dominates the boiling process. This is not unexpected because in the theory of Berenson, the average height of the bubble must be less than the bubble diameter. This assumption is greatly violated as the bubble release process is transformed into jet flow. The figure also shows that the calculations and the theories have different trend in the variation of the Nusselt number with the superheat. The correlation curves decrease monotonically with the superheated temperature, but not the calculations. The cause of the decrease of the theories is mainly ascribed to the great decrease in Prandtl number and the great increase in Jacob number, despite

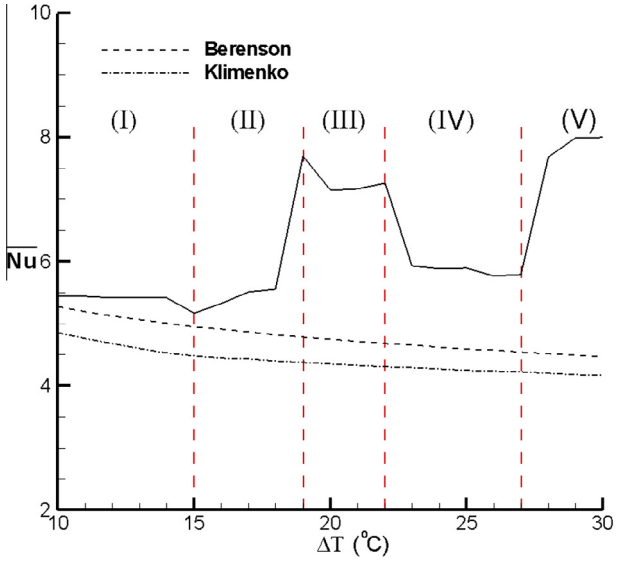

Fig. 11. Variation of mean Nusselt number against superheated temperature with five boiling modes being identified: (I) single bubble; (II) single/multiple bubble; (III) single jet; (IV) double bubble; (V) double jet.

Table 1
Comparison of Nusselt number.

	$\Delta T = 10$ °C	$\Delta T = 18$ °C	$\Delta T = 20$ °C	$\Delta T = 25$ °C	$\Delta T = 30$ °C	$\Delta T = 40$ °C
$(Nu)_{comp}$	5.43	5.55	7.14[a]	5.89	8.0[a]	8.07[a]
$(Nu)_{Ber}$	5.27	4.82	4.75	4.59	4.47	4.28
$(Nu)_{Klim}$	4.85	4.40	4.35	4.25	4.17	4.03

[a] Average over the jet-pattern period.

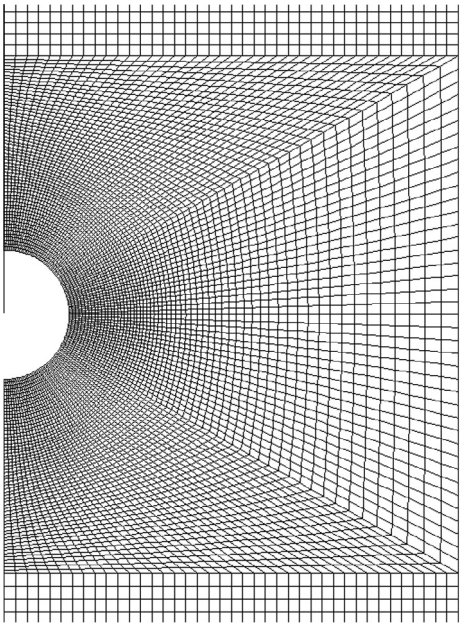

Fig. 12. A typical grid arrangement around the cylinder.

the slight increase in Grashof number, when the temperature is increased.

4.4. Film boiling on a cylindrical surface

Most methods developed in the past for two-fluid flow calculations are formulated on Cartesian grids. In order to deal with flows with irregular boundaries, these methods require modification. As an example, the level set method was modified by Son [31] to include immersed solid objects. It can be seen that the method presented in this study is applicable to unstructured grids of arbitrary topology. Therefore, it is suitable to problems with complex geometry. This feature is demonstrated in this boiling flow problem with an immersed cylindrical film.

The same state of near critical point is considered. The diameter D (=0.213 mm) of the cylinder is taken to equal to a reference length $\lambda = \sqrt{\sigma/(\rho_l - \rho_v)g}$. The domain has a width of 7D and a height of 15D. The center of the cylinder is placed at a location (3.5D, 3.5D). Due to the geometrical symmetry, only half of the domain is required in the computation. Slip conditions are imposed at all the boundaries except the top one, which is treated as an open boundary. Initially, the film around the cylinder is uniformly distributed with a thickness of 0.1D. Three different meshes with 12200, 48800, and 109800 nodes were used in grid sensitivity tests. It was found that the grid of medium density is fine enough for calculations. A layout of the coarsest grid in the region near the cylinder is illustrated in Fig. 12.

Fig. 13(a) shows the evolution of the bubble growth and release process for superheat of 10 °C. It is visible that after the bubble is detached, the surface tension drags the vapor stem downward, causing a surface wave to be formed on the interface of the film.

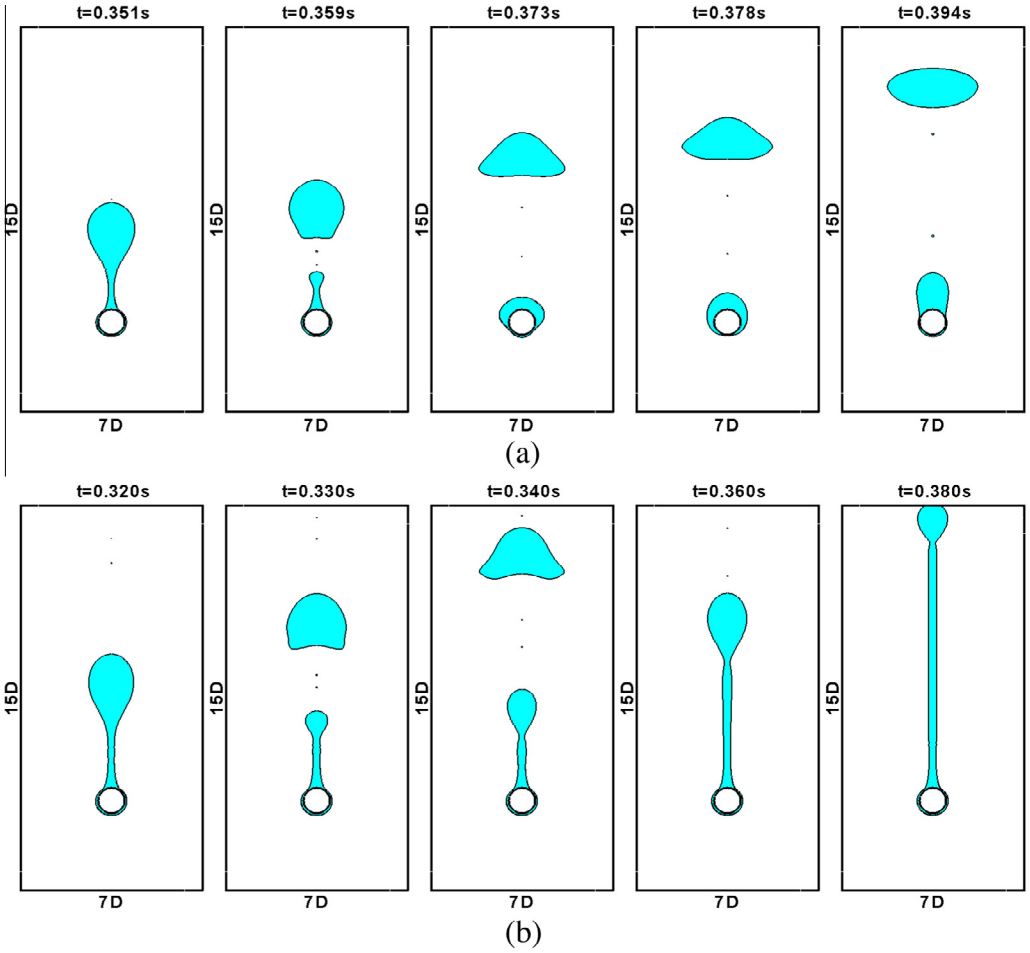

Fig. 13. Circular film boiling process: (a) ΔT = 10 °C; (b) ΔT = 30 °C.

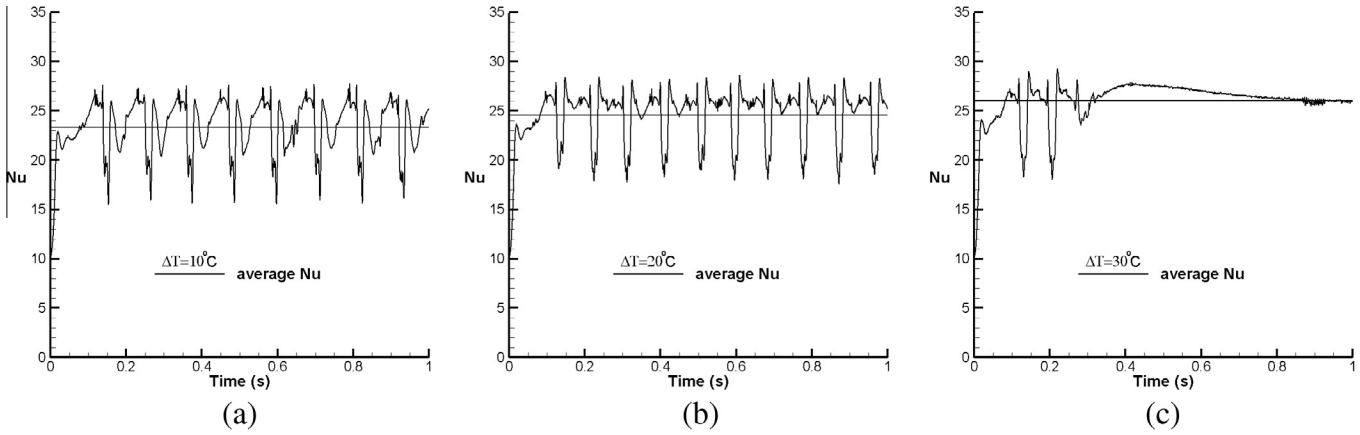

Fig. 14. Variation of Nusselt number for circular film boiling: (a) ΔT = 10 °C; (b) ΔT = 20 °C; (c) ΔT = 30 °C.

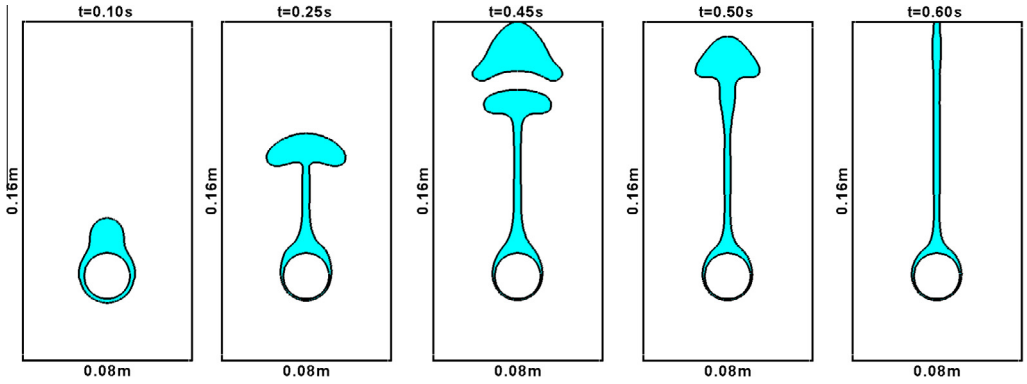

Fig. 15. Circular film boiling process for the macroscale cylinder case.

Periodic formation and release of the bubble becomes a routine pattern at low superheats. As the temperature difference is increased to 30 °C, it is seen from Fig. 13(b) that after the vapor bubble is separated, the stem continues to grow and elongate. In the end, a jet is formed.

The above phenomena can also be identified from the evolution of the mean Nusselt number shown in Fig. 14. As expected, the Nusselt number varies in a periodic way for ΔT = 10 °C. The time period is about 0.11 s. As the temperature difference is increased to 20 °C, the cyclic pattern remains, but with a decrease of the time period to 0.095 s. Further increase of ΔT to 30 °C leads to a vapor jet and, thus, a smooth variation of the Nusselt number.

Bromley [32] presented a model for saturated film boiling on a horizontal cylinder based on boundary layer theory. The correlation for Nusselt number is of the similar form as Eq. (28) with the diameter D as the characteristic length and the constant C is given as 0.62. Based on this theory, the resulting Nusselt numbers for ΔT = 10, 20 and 30 °C are 7.69, 6.92, and 6.52, respectively. It is worthy to mention that the modified Jacob number Ja^* is used in the calculation. The computed values in our simulations are 23.3, 24.6, and 26.0, which are much higher than the Bromley's model. One of the factors to affect the simulation accuracy is the large variation of vapor properties with temperature at this near critical point state. In the simulation, these properties are fixed at the saturated temperature. It was reported by Agarwal et al. [9] that the Nusselt number is reduced by 37% when the effect of temperature on thermal properties is taken into account. Another factor contributed to the large deviation may be ascribed to the microscale diameter of the cylinder (D = 0.21 mm). In the study of Son and Dhir [33], three-dimensional calculations were performed for the film boiling on horizontal cylinder at atmospheric pressure. Different sizes of cylinder diameter were under test: 0.125, 1.25, and 12.5 mm. It was seen that large difference in Nusselt number exists for the smallest cylinder (D = 0.125 mm). The computed Nu is 5.4, compared to 2.84 obtained from Bromley's correlation. The correlation value should be even smaller (1.76) because we had checked to find out that the constant 0.62 of the correlation was missing in the results of Son and Dhir.

In order to confirm the above discussion, we consider a case with a cylinder of macroscale diameter 21.6 mm (=3λ). The saturation pressure of the considered fluid is 1 atm (P_{sat} = 1.0135 × 10^5 - Pa) and the saturation temperature T_{sat} = 227 °C. The liquid properties used are ρ_l = 200 kg/m^3, k_l = 40 W/(m-K), μ_l = 0.1 Pa-s, C_l = 0.4 kJ/kg-K and those for the vapor phase are ρ_v = 5 kg/m^3, k_v = 1 W/(m-K), μ_v = 0.01 Pa-s, C_v = 0.2 kJ/kg-K. The latent heat is h_{lv} = 10 kJ/kg and the surface tension σ = 0.1 N/m. The wall is superheated at 5 °C higher than the saturation temperature. This two-phase fluid was adopted by Welch and Wilson [7] in their simulations for film boiling on a horizontal flat plate. Fig. 15 shows that after a bubble is released, a vapor jet is formed. This boiling pattern is similar to the simulation of Esmaeeli and Tryggvason [34]. The calculated Nusselt number in the steady jet state is 11.04, which is 50% higher than the correlation value 7.37, compared to the more than 3 times higher in the microscale case.

5. Conclusions

The CISIT method is a VOF variant aiming at tracking the interface between two fluids. This approach was modified to include heat and mass transfer in this study to deal with two-phase boiling

flows. In the model, the interface is regarded as an internal boundary. The heat fluxes at the boundary are calculated separately in individual phases and then the energy equation for the entire flow field is solved implicitly. Comparison of the calculations with theoretical solutions of 1-D model problems indicates good agreement.

The method was first applied to examine the boiling flow with a planar film at a state near the critical pressure. Five different boiling modes were detected, depending on the wall superheat. In the single-bubble mode at low superheats, periodic release of a single bubble occurs on either side of the boundary. It is, then, changed to the single/multiple-bubble mode with a single bubble formed on one side and multiple bubbles formed on the other. Further increase of the superheat results in formation a vapor jet on one side (single-jet mode). It is followed by a double-bubble mode in which two consecutive bubbles are developed on the two side boundaries. When the superheat is high enough, vapor jet is found on both sides (double-jet mode), rendering the flow steady. Good agreement with semi-empirical correlations was obtained in terms of averaged Nusselt number in the single-bubble mode, and reasonable agreement in the single/multiple-bubble mode. When the jet flow pattern appear, the difference becomes significant, with the calculated value much higher.

The boiling flow on a cylinder was also under consideration to show that this scheme is applicable to problems with complex geometry. Similar to the flat plane case, bubble release pattern is seen at low superheats whereas vapor jet is developed as the superheated temperature is high enough. The computed Nusselt number is much higher than the model correlations, which is mainly due to the microscale of the cylinder.

Acknowledgements

This work was supported by the National Science Council of ROC under the Contract Numbers NSC 98-2221-E-009-130 and NSC 101-2221-E009-044.

References

[1] S.W.J. Welch, Local simulation of two-phase flows including interface tracking with mass transfer, J. Comput. Phys. 121 (1995) 142–154.
[2] S.W.J. Welch, Direct simulation of vapor bubble growth, Int. J. Heat Mass Transfer 41 (1998) 1655–1666.
[3] G. Son, V.K. Dhir, Numerical simulation of saturated film boiling on a horizontal surface, ASME J. Heat Transfer 119 (1997) 525–533.
[4] D. Juric, G. Tryggvason, Computations of boiling flows, Int. J. Multiphase flow 24 (1998) 387–410.
[5] A. Esmaeeli, G. Tryggvason, Computations of film boiling. Part I: numerical method, Int. J. Heat Mass Transfer 47 (2004) 5451–5461.
[6] G. Tryggvasson, B. Bunner, A. Esmaeeli, D. Juric, N. Al-Rawahi, W. Tauber, J. Han, S. Nas, Y.-J. Jan, A front-tracking method for the computations of multiphase flow, J. Comput. Phys. 169 (2001) 708–759.
[7] S.W.J. Welch, J. Wilson, A volume of fluid based method for fluid flows with phase change, J. Comput. Phys. 160 (2000) 662–682.
[8] S.W.J. Welch, T. Rachidi, Numerical computation of film boiling including conjugate heat transfer, Numer. Heat Transfer, Part B: Fundam. 42 (2002) 35–53.
[9] D.K. Agarwal, S.W.J. Welch, G. Biswas, F. Durst, Planar simulation of bubble growth in film boiling in near-critical water using a variant of the VOF method, ASME J. Heat Transfer 126 (2004) 329–338.
[10] G. Son, V.K. Dhir, Numerical simulation of film boiling near critical pressures with a level set method, ASME J. Heat Transfer 120 (1998) 183–192.
[11] G. Son, V.K. Dhir, N. Ramanujapu, Dynamics and heat transfer associated with a single bubble during nucleate boiling on a horizontal surface, ASME J. Heat Transfer 121 (1999) 623–631.
[12] G. Son, A numerical method for bubble motion with phase change, Numer. Heat Transfer, Part B: Fundam. 39 (2001) 509–523.
[13] M. Sussman, E. Fatami, P. Smereka, S. Osher, An improved level set method for incompressible two-phase flows, Comput. Fluids 27 (1998) 663–680.
[14] R.P. Fedkiw, T. Aslam, B. Merriman, S. Osher, A non-oscillatory Eulerian approach to interfaces in multimaterial flows (the ghost fluid method), J. Comput. Phys. 152 (1999) 457–492.
[15] M. Kang, R.P. Fedkiw, X.-D. Liu, A boundary condition capturing method for multiphase incompressible flow, SIAM J. Sci. Comput. 15 (2000) 323–360.
[16] S. Tanguy, T. Menard, A. Berlemont, A level set method for vaporizing two-phase flows, J. Comput. Phys. 221 (2007) 837–853.
[17] F. Gibou, L. Chen, D. Nguyen, S. Banerjee, A level set based sharp interface method for the multiphase incompressible Navier–Stokes equations with phase change, J. Comput. Phys. 222 (2007) 536–555.
[18] G. Son, V.K. Dhir, A level set method for analysis of film boiling on an immersed solid surface, Numer. Heat Transfer, Part B: Fundam. 52 (2007) 153–177.
[19] R.S. Maurya, S.V. Diwakar, T. Sundararajan, S.K. Das, Numerical investigation of evaporation in the developing region of laminar falling film flow under constant wall heat flux conditions, Numer. Heat Transfer, Part A: Appl. 58 (2010) 41–64.
[20] D.Z. Guo, D.L. Sun, Z.Y. Li, W.Q. Tao, Phase change heat transfer simulation for boiling bubbles arising from a vapor film by the VOSET method, Numer. Heat Transfer, Part A: Appl. 59 (2011) 857–881.
[21] Y.-Y. Tsui, S.-W. Lin, A VOF based conservative interpolation scheme for interface tracking (CISIT) of two-fluid flows, Numer. Heat Transfer, Part B: Fundam. 63 (2013) 263–283.
[22] J.U. Brackbill, D.B. Kothe, C. Zemach, A continuum method for modeling surface tension, J. Comput. Phys. 100 (1992) 335–354.
[23] D.L. Youngs, Time-dependent multi-material flow with large fluid distortion, in: K.W. Morton, M.J. Baines (Eds.), Numerical Methods for Fluid Dynamics, Academic Press, New York, 1982, pp. 273–285.
[24] Y.-Y. Tsui, Y.-F. Pan, A pressure-correction method for incompressible flows using unstructured meshes, Numer. Heat Transfer, Part B: Fundam. 49 (2006) 43–65.
[25] Y.-Y. Tsui, T.-C. Wu, A pressure-based unstructured-grid algorithm using high resolution schemes for all-speed flows, Numer. Heat Transfer, Part B: Fundam. 53 (2008) (2008) 75–96.
[26] Y.-Y. Tsui, S.-W. Lin, T.-T. Cheng, T.-C. Wu, Flux-blending schemes for interface capture in two-fluid flows, Int. J. Heat Mass Transfer 52 (2009) 5547–5556.
[27] Y.-Y. Tsui, Y.-C. Huang, C.-L. Huang, S.-W. Lin, A finite-volume based approach for dynamic fluid-structure interaction, Numer. Heat Transfer, Part B: Fundam. 64 (2013) 326–349.
[28] V. Alexiades, A.D. Solomon, Mathematical Modeling of Melting and Freezing Processes, first ed., Hemisphere, Washington, D.C., 1993.
[29] P.J. Berenson, Film-boiling heat transfer from a horizontal surface, ASME J. Heat Transfer 83 (1961) 351–358.
[30] V.V. Klimenko, Film-boiling on a horizontal plate – new correlation, Int. J. Heat Mass Transfer 24 (1981) 69–79.
[31] G. Son, A level set method for incompressible two-fluid flows with immersed solid boundaries, Numer. Heat Transfer, Part B: Fundam. 47 (2005) 473–489.
[32] L.A. Bromley, Heat transfer in stable film boiling, Chem. Eng. Progr. 46 (1950) 221–227.
[33] G. Son, V.K. Dhir, Three-dimensional simulations of saturated film boiling on a horizontal cylinder, Int. J. Heat Mass Transfer 51 (2008) 1156–1167.
[34] A. Esmaeeli, G. Tryggvason, A front tracking method for computations of boiling in complex geometries, Int. J. Multiphase Flow 30 (2004) 1037–1050.